

Colossal Barocaloric Effects with Ultralow Hysteresis in Two-Dimensional Metal–Halide Perovskites

Jarad Mason (✉ mason@chemistry.harvard.edu)

Harvard University <https://orcid.org/0000-0003-0328-7775>

Jinyoung Seo

Harvard University

Ryan McGillicuddy

Harvard University

Adam Slavney

Harvard University

Selena Zhang

Harvard University

Andrey Yakovenko

Argonne National Laboratory

Shao-Liang Zheng

Harvard University <https://orcid.org/0000-0002-6432-9943>

Letter

Keywords: alternative cooling technologies, barocaloric materials, hydrocarbon chain-melting, two-dimensional metal–halide perovskites

Posted Date: August 16th, 2021

DOI: <https://doi.org/10.21203/rs.3.rs-426701/v1>

License: © ⓘ This work is licensed under a Creative Commons Attribution 4.0 International License.

[Read Full License](#)

Version of Record: A version of this preprint was published at Nature Communications on May 9th, 2022. See the published version at <https://doi.org/10.1038/s41467-022-29800-9>.

Colossal Barocaloric Effects with Ultralow Hysteresis in Two-Dimensional Metal–Halide Perovskites

Jinyoung Seo,¹ Ryan D. McGillicuddy,¹ Adam H. Slavney,¹ Selena Zhang,¹
Andrey A. Yakovenko,² Shao-Liang Zheng¹ & Jarad A. Mason^{1*}

¹Department of Chemistry and Chemical Biology, Harvard University, Cambridge, Massachusetts 02138, United States. ²X-ray Science Division, Advanced Photon Source, Argonne National Laboratory, Argonne, Illinois 60439, United States.

Nearly 4,400 TWh of electricity—20% of the total consumed in the world—is used each year by refrigerators, air conditioners, and heat pumps for cooling¹. In addition to the 2.3 Gt of carbon dioxide emitted during the generation of this electricity, the vapor-compression-based devices that provided the bulk of this cooling emitted fluorocarbon refrigerants with a global warming potential equivalent to 1.5 Gt of carbon dioxide into the atmosphere². With population and economic growth expected to dramatically increase over the next several decades, the development of alternative cooling technologies with improved efficiency and reduced emissions will be critical to meeting global cooling needs in a more sustainable fashion³. Barocaloric materials, which undergo thermal changes in response to applied hydrostatic pressure, offer the potential for solid-state cooling with high energy efficiency and zero direct emissions, as well as faster start-up times, quieter operation, greater amenability to miniaturization, and better recyclability than conventional vapor-compression systems^{4,5}. Efficient barocaloric cooling requires materials that undergo reversible phase transitions with large entropy changes, high sensitivity to hydrostatic pressure, and minimal hysteresis, the combination of which has been challenging to achieve in existing barocaloric materials. Here, we report a new mechanism for achieving colossal barocaloric effects near ambient temperature that exploits the large volume and conformational entropy changes of hydrocarbon chain-melting transitions within two-dimensional metal–halide perovskites. Significantly, we show how the confined nature of these order–disorder phase transitions and the synthetic tunability of layered perovskites can be leveraged to reduce phase transition hysteresis through careful control over the inorganic–organic interface. The combination of ultralow hysteresis (< 1.5 K) and high barocaloric coefficients (> 20 K kbar⁻¹) leads to large reversible isothermal entropy changes (> 200 J kg⁻¹ K⁻¹) at record-low pressures (< 300 bar). We anticipate that these results will

25 **help facilitate the development of barocaloric cooling technologies and further inspire new**
materials and mechanisms for efficient solid-state cooling.

Caloric effects are particularly strong in ferroic materials near first-order phase transitions, where small changes to the magnitude of an applied field can induce the large isothermal entropy and adiabatic temperature changes required for commercially viable cooling cycles⁶⁻⁸. An ideal material for barocaloric cooling would feature a phase transition with *i*) a large isothermal entropy change (ΔS_{it}) and adiabatic temperature change (ΔT_{ad}), *ii*) a large barocaloric coefficient (dT_{tr}/dP) that reflects a high sensitivity of the transition temperature, T_{tr} , to pressure, P , and *iii*) a low reversible pressure, P_{rev} , which represents the minimum pressure required to induce a reversible entropy change and is proportional, in part, to the thermal hysteresis of the phase transition⁹.
30 Among the limited range of compounds that have been investigated as candidate barocaloric materials, certain organic plastic crystals, such as neopentylglycol, have recently been shown to exhibit order–disorder phase transitions in the solid state that yield colossal barocaloric effects with entropy changes approaching those of commercial hydrofluorocarbon refrigerants⁹⁻¹¹. These transitions, however, often have large thermal hysteresis, occur away from ambient temperature,
35 or have only moderate sensitivity to applied pressure. This highlights a longstanding challenge across all classes of caloric materials: field-induced phase transitions that lead to large isothermal entropy and adiabatic temperature changes are often accompanied by substantial hysteresis, which increases the magnitude of the applied field required to capture the full entropy of the transition and reduces the efficiency of each cooling cycle¹²⁻¹⁵.
40

45 In pursuit of a new strategy to target barocaloric effects with low hysteresis, high sensitivity to pressure, and large entropy changes near ambient temperature, we sought a phase transition mechanism that would offer access to large volume changes and disordered states with high entropy but could take place within a microenvironment tailored to promote reversibility. To this end, we recognized that long-chain hydrocarbons undergo order–disorder transitions with far
50 higher entropy changes than have ever been realized in a caloric effect. For instance, the entropy of *n*-decane ($C_{10}H_{22}$) increases by $829 \text{ J kg}^{-1} \text{ K}^{-1}$ ($118 \text{ J mol}^{-1} \text{ K}^{-1}$) upon melting¹⁶, which is even larger than the $520 \text{ J kg}^{-1} \text{ K}^{-1}$ ($53 \text{ J mol}^{-1} \text{ K}^{-1}$) increase in entropy of the commercial refrigerant HFC-134a (CH_2FCF_3) upon vaporization¹⁷. These high entropy changes arise from increases in orientational, conformational, and positional entropy as molecules restricted in the crystalline state
55 gain access to more rotational, vibrational, and translational degrees of freedom in the disordered—and expanded—molten state¹⁸.

The entropy and latent heat changes associated with hydrocarbon melting transitions are already exploited for thermal energy storage in paraffin-based solid–liquid phase-change materials¹⁹. Although they have not yet received attention in barocaloric materials, similar types of chain-melting transitions are known to occur in the solid state in several classes of layered materials, including two-dimensional (2-D) metal–halide perovskites of the form $(\text{R-NH}_3)_2\text{MX}_4$ ($\text{R} = \text{C}_n\text{H}_{2n+1}$; $\text{M} = \text{Mn, Fe, Cu, Cd, Pb}$; $\text{X} = \text{Cl, Br, or I}$)^{20,21}. In these compounds, sheets of corner-sharing MX_6 octahedra create anionic pockets—defined by the axial halides of four adjacent metal centers—that template the arrangement of bilayers of alkylammonium cations through charge-assisted hydrogen bonds. When long-chained hydrocarbon molecules ($n > 3$) are incorporated, many layered perovskites undergo thermally induced, first-order phase transitions between ordered and disordered states driven by what is effectively a partial melting transition of the hydrocarbon bilayers (Supplementary Tables 1–3). As such, we anticipated that 2-D perovskites would serve as a highly tunable solid-state platform to leverage the large changes in entropy and enthalpy that accompany hydrocarbon chain-melting transitions for barocaloric cooling (Fig. 1a). Moreover, since the inorganic layers and organic bilayers of 2-D perovskites can be independently manipulated, we further expected that phase transition hysteresis could be minimized through confinement effects and careful control of the organic–inorganic interfaces.

The 2-D perovskite $(\text{DA})_2\text{MnCl}_4$ ($\text{DA} = \text{decylammonium}$) was selected as a potential barocaloric material because of its large phase-transition entropy ($\Delta S_{\text{tr}} = 230 \text{ J kg}^{-1} \text{ K}^{-1}$) and enthalpy ($\Delta H_{\text{tr}} = 71 \text{ kJ kg}^{-1}$), near-ambient phase transition temperature ($T_{\text{tr}} = 310 \text{ K}$), and lightweight, nontoxic elemental composition (Figs. 1b, 4a). At ambient temperature and pressure, $(\text{DA})_2\text{MnCl}_4$ adopts an ordered monoclinic structure (low-temperature, LT, phase) with bilayers of hydrocarbon chains—each of which contains a single gauche C–C bond (C2–C3) and seven trans C–C bonds—aligned parallel to one another and tilted $48.3(1)^\circ$ with respect to the Mn-Cl_{eq} plane (Fig. 2e)²². Upon heating above 310 K, the compound undergoes a first-order phase transition to an expanded orthorhombic lattice (high-temperature, HT, phase) with disordered hydrocarbon chains that have liquid-like conformational degrees of freedom²³. The large increase in entropy during the transition can be attributed to both flipping of the alkylammonium cations between two favorable orientations within the Mn-Cl pockets and internal rotations of C–C bonds that create dynamically disordered conformational defects within the hydrocarbon chains²⁴.

Differential scanning calorimetry (DSC) measurements at ambient pressure show that the hydrocarbon chain-melting transition is sharp and fully reversible with a thermal hysteresis, ΔT_{hys} ,

of just 1.4 K at a scan rate of 2 K min⁻¹ (Fig. 2a). Variable temperature powder X-ray diffraction (PXRD) experiments at ambient pressure show that the phase transition is accompanied by an increase in interlayer distance of 1.88 Å (7.0%) as the alkylammonium cations tilt further away from the Mn–Cl_{eq} plane to create additional space between disordered hydrocarbon chains in the HT phase (Supplementary Fig. 18). This expansion leads to an 8.0% overall increase in the volume of the compound ($\Delta V_{\text{tr}} = 65.9 \text{ cm}^3 \text{ kg}^{-1}$; Fig. 2c). Based on the measured volume and entropy changes, the Clausius–Clapeyron equation, $dT_{\text{tr}}/dP = \Delta V_{\text{tr}}/\Delta S_{\text{tr}}$, can be used to predict a barocaloric coefficient for (DA)₂MnCl₄ of 28.7 K kbar⁻¹, which would represent one of the highest values reported for a barocaloric material (Extended Data Table 1).

To directly evaluate the pressure dependence of the phase transition temperature, isobaric DSC experiments were performed under applied hydrostatic pressures of up to 150 bar using He as the pressure-transmitting medium. As expected, the phase transition shifts to higher temperatures as the pressure is increased, with a measured dT_{tr}/dP of $22.1 \pm 0.7 \text{ K kbar}^{-1}$ during heating and $20.6 \pm 0.8 \text{ K kbar}^{-1}$ during cooling (Figs. 3a, h). Importantly, the application of pressure does not lead to any significant changes to the phase transition width, and ΔS_{tr} remains within 97% of its ambient pressure value at 150 bar (Supplementary Fig. 2). Variable temperature and pressure PXRD experiments (performed at beamline 17-BM of the Advanced Photon Source at Argonne National Laboratory) confirm that chain-melting transitions still occur at pressures up to at least 360 bar (Fig. 3g, Supplementary Figs. 8 and 9, Extended Data Fig. 3), with small decreases in overall volume changes at higher pressures that are consistent with a higher compressibility for the HT phase relative to the LT phase (Supplementary Table 7). Importantly, the measured dT_{tr}/dP of $18.8 \pm 2.1 \text{ K kbar}^{-1}$ during cooling over this extended pressure range is in close agreement with that determined by HP-DSC (Fig. 3h).

Interestingly, the dT_{tr}/dP values for (DA)₂MnCl₄ determined by PXRD and HP-DSC are lower than those predicted using the Clausius–Clapeyron equation. One possible explanation for this is that the effective volume change in the presence of a pressure-transmitting medium is less than the crystallographic volume change²⁵. This could occur if He was excluded from the dense, crystalline organic bilayer of the LT phase but could permeate into the disordered organic bilayer of the HT phase—owing to its increased free volume—which would reduce the amount of additional volume that was occupied by the expanded phase. Indeed, the volume change that is directly measured by He pycnometry is $17 \text{ cm}^3 \text{ kg}^{-1}$ smaller than that determined by crystallography (Fig. 2c), and using this lower effective volume change in the Clausius–Clapeyron equation yields a predicted dT_{tr}/dP

of $21.4 \pm 1.5 \text{ K kbar}^{-1}$ that matches the HP-DSC and PXRD values (Supplementary Table 10). Although effects of the pressure-transmitting medium are not typically considered when evaluating barocaloric materials, this result provides a pathway to realizing a higher dT_{tr}/dP by preventing the pressure-transmitting medium from entering the disordered phase through encapsulation or the use of a more sterically bulky fluid. Regardless, the dT_{tr}/dP that can be achieved using He to transmit hydrostatic pressure is higher than for many barocaloric materials, which, along with the large ΔS_{tr} and small hysteresis, presents considerable advantages for barocaloric cooling.

Under the cyclic operating conditions of a barocaloric cooling system, the lowest possible operating pressure will be set by the pressure that must be applied to induce a reversible entropy change, P_{rev} , when cycling to and from ambient pressure. For a normal barocaloric effect, P_{rev} corresponds to the pressure at which the onset temperature of the exothermic phase transition is equal to the onset temperature of the endothermic phase transition at 1 bar (ref. 9). As such, P_{rev} is proportional to the thermal hysteresis at 1 bar and inversely proportional to the barocaloric coefficient for the exothermic transition, with $P_{\text{rev}} = \Delta T_{\text{hys}} / (dT_{\text{tr}}/dP)_{\text{cooling}}$. Owing to its low ΔT_{hys} and high dT_{tr}/dP , $(\text{DA})_2\text{MnCl}_4$ has a predicted P_{rev} of just 66 bar, which ranks among the lowest values reported for barocaloric materials (Fig. 4b, Extended Data Table 1).

This low P_{rev} was further confirmed by calculating isothermal entropy changes (ΔS_{it}) as a function of temperature and pressure from the difference between isobaric entropy changes, ΔS_{ib} , at ambient pressure and elevated pressures. Here, ΔS_{ib} values obtained from heating data correspond to the disordering transition induced by a decrease in pressure ($\Delta S_{\text{it}} > 0$), while ΔS_{ib} values from cooling data correspond to the ordering transition induced by an increase in pressure ($\Delta S_{\text{it}} < 0$) (Supplementary Fig. 4). Excitingly, these ΔS_{it} curves confirm that a non-zero reversible entropy change can be induced below 80 bar (Fig. 3b). Moreover, a reversible entropy change of $75 \text{ J kg}^{-1} \text{ K}^{-1}$ can be accessed at a driving pressure of 150 bar, and the full entropy of the chain-melting transition should become reversible at only 280 bar (Extended Data Fig. 1). To the best of our knowledge, inducing a reversible entropy change of more than $200 \text{ J kg}^{-1} \text{ K}^{-1}$ through a pressure change of less than 300 bar is unprecedented in barocaloric materials (Extended Data Table 1). As a result, $(\text{DA})_2\text{MnCl}_4$ displays a record-high barocaloric strength—the reversible isothermal entropy change normalized by the driving pressure²⁶—of $500 \text{ J kg}^{-1} \text{ K}^{-1} \text{ kbar}^{-1}$ at 150 bar (Extended Data Table 2). Assuming an average specific heat capacity, c_p , of $1550 \text{ J kg}^{-1} \text{ K}^{-1}$ across the phase transition and that c_p does not vary substantially with pressure (Supplementary Fig. 6), a maximum adiabatic temperature change, $\Delta T_{\text{ad,max}}$, of 43 K can be

estimated from $T_{ad,max} = T\Delta S_{it} / c_p$, which ranks among the highest values yet reported for barocaloric materials (Extended Data Table 2).

155 Although quasi-direct methods of calculating isothermal changes—and adiabatic changes—
from isobaric experiments are commonly used to evaluate barocaloric materials due to the
challenge of maintaining isothermality—or adiabaticity—during direct variable pressure
measurements²⁶, we also performed quasi-isothermal HP-DSC experiments to more directly
evaluate P_{rev} by measuring pressure hysteresis. Specifically, we measured heat flow signals while
160 cycling between 1 bar and 150 bar at 311 K. By comparing the onset pressures for compression-
induced exotherms and decompression-induced endotherms, we were able to directly measure a
pressure hysteresis of 70 bar for $(DA)_2MnCl_4$, which is in excellent agreement with the predicted
value of 73 bar at 311 K (Fig. 3c, Extended Data Fig. 2).

In an effort to target barocaloric materials with large reversible entropy changes at even lower
165 pressures, we searched for a 2-D perovskite that undergoes a chain-melting transition near ambient
temperature with a thermal hysteresis of less than 1 K. Unlike $(DA)_2MnCl_4$, however, the total
entropy of the chain-melting transition in most 2-D perovskites is partitioned across one or more
minor—lower entropy—phase transitions in addition to the principal transition (Fig. 1b,
Supplementary Tables 1–3). Although not necessarily detrimental to barocaloric cooling
170 performance²⁷, the presence of multiple successive transitions at different temperatures
complicates the evaluation of barocaloric properties because each minor and major transition has
an independent hysteresis loop—often greater than 1 K—with different pressure dependences
(Supplementary Tables 4). With a lack of suitable existing compounds, we endeavored to
synthesize a new 2-D perovskite that features a sharp chain-melting transition near ambient
175 temperature with ultralow hysteresis and a high sensitivity to pressure.

After screening different combinations of metal cations, halide anions, and alkylammonium
chain lengths, we found that the new 2-D perovskite $(NA)_2CuBr_4$ (NA = nonylammonium)
undergoes a chain melting transition at 305 K with a high ΔS_{tr} ($76 \text{ J kg}^{-1} \text{ K}^{-1}$) and hysteresis of
only 0.4 K (Fig. 2b). Variable-temperature PXRD experiments, combined with single-crystal
180 structures at 270 K and 335 K, revealed that the phase transition involves a 4.0% increase in
volume ($\Delta V_{tr} = 25.3 \text{ cm}^3 \text{ kg}^{-1}$) and a 2.9% (0.67 \AA) increase in interlayer distance (Fig. 2g). The
crystallographic volume change yields a predicted barocaloric coefficient of 33.3 K kbar^{-1} , while
the volume change determined by He pycnometry ($\Delta V_{tr} = 20.0 \text{ cm}^3 \text{ kg}^{-1}$)—which accounts for He

permeation—yields a predicted barocaloric coefficient of $26.3 \pm 2.5 \text{ K kbar}^{-1}$ (Fig. 2d, Supplementary Table 10).

Isobaric HP-DSC experiments confirmed that $(\text{NA})_2\text{CuBr}_4$ features high barocaloric coefficients of $26.9 \pm 0.4 \text{ K kbar}^{-1}$ and $26.5 \pm 0.5 \text{ K kbar}^{-1}$ during heating and cooling, respectively (Figs. 3d, j). In fact, these values represent one of the highest sets of barocaloric coefficients ever measured (Extended Data Table 1). In addition, variable pressure PXRD experiments show that the chain-melting transition persists to at least 300 bar with a similar volume change ($21\text{--}25 \text{ cm}^3 \text{ kg}^{-1}$) and average barocaloric coefficient ($25.9 \pm 3.2 \text{ K kbar}^{-1}$) (Figs. 3i, j, Supplementary Figs. 10–12, Extended Data Fig. 4). As a result of its high barocaloric coefficient and ultralow hysteresis, $(\text{NA})_2\text{CuBr}_4$ has, to the best of our knowledge, the lowest reported P_{rev} for a barocaloric material of 16 bar (Fig. 4b), which is within the pressure range already accessed during commercial vapor-compression refrigeration cycles¹⁷. The low value of P_{rev} was further confirmed through quasi-isothermal pressure cycling experiments at 307 K, where we directly measured a pressure hysteresis of 25 bar (Fig. 3f). Moreover, a reversible entropy change of $68 \text{ J kg}^{-1} \text{ K}^{-1}$ (90% of ΔS_{tr} at 1 bar) can be accessed at a driving pressure of just 150 bar (Fig. 3e, Extended Data Fig. 1), yielding a barocaloric strength of $453 \text{ J kg}^{-1} \text{ K}^{-1} \text{ kbar}^{-1}$ (Extended Data Table 2).

To provide additional insight into the structural and chemical factors that influence barocaloric effects in 2-D perovskites, we used X-ray crystallography and infrared (IR) spectroscopy to compare the nature of the chain-melting transition in $(\text{NA})_2\text{CuBr}_4$ and $(\text{DA})_2\text{MnCl}_4$. In particular, we hypothesized that the increased size of the halide pocket in $(\text{NA})_2\text{CuBr}_4$ (30.5 \AA^2) relative to $(\text{DA})_2\text{MnCl}_4$ (26.3 \AA^2)—coupled with weaker N–H \cdots Br hydrogen bonds at the organic–inorganic interface—would lead to increased free volume in the organic bilayer of the Cu compound and, as a result, greater disorder in the LT phase. As anticipated, the atoms in the NA chains of $(\text{NA})_2\text{CuBr}_4$ have much larger atomic displacement parameters in the LT phase than those in the DA chains of the LT phase of $(\text{DA})_2\text{MnCl}_4$ (Figs. 2f, h, Extended Data Fig. 5). This is consistent with the LT phase of $(\text{NA})_2\text{CuBr}_4$ having increased vibrational and conformational degrees of freedom, which would reduce the entropy difference between the LT and HT phases.

The increased entropy of the alkylammonium chains of $(\text{NA})_2\text{CuBr}_4$ prior to the chain-melting transition is further corroborated by a broad feature in the heat capacity from 220–250 K that is consistent with a gradual activation of conformational degrees of freedom from the fully ordered organic bilayer that is present at 100 K (Supplementary Fig. 19, Extended Data Fig. 6). Variable-

temperature IR spectra are also consistent with increased conformational entropy for the hydrocarbon chains in the LT phase of (NA)₂CuBr₄. Specifically, IR spectra show a band near 1360 cm⁻¹, which can be assigned to CH₂ wagging from *gt*_{2n+1}*g'*-type kinks, that is present below the phase transition temperature for (NA)₂CuBr₄ but only above the phase transition temperature for (DA)₂MnCl₄ (Extended Data Fig. 7). As discussed in greater detail in the supplementary text, the IR spectra also suggest that the local environment around the chain ends (CH₃) and headgroups (NH₃⁺) is more similar in the LT and HT phases of (NA)₂CuBr₄ than in those of (DA)₂MnCl₄ (Supplementary Table 5).

Although increasing the halide pocket size through Br substitution leads to a decreased entropy change (Fig. 4a), it also likely contributes to the enhanced reversibility of the (NA)₂CuBr₄ chain-melting transition through two primary effects. First, the softer nature of Br anions—along with the higher degree of disorder in the alkylammonium chains in the LT phase—makes the (NA)₂CuBr₄ lattice more compressible than the (DA)₂MnCl₄ lattice (Supplementary Table 6). Since the barocaloric coefficient dT_{tr}/dP of a solid tends to increase with increasing compressibility^{10,28}, this causes the phase transition in (NA)₂CuBr₄ to be more sensitive to pressure, which reduces the minimum pressure required to overcome hysteresis and induce a reversible phase transition. Indeed, dT_{tr}/dP for the compression-induced transition in (NA)₂CuBr₄ is 29% higher than for (DA)₂MnCl₄. Second, the increased free volume and presence of additional vibrational and conformational degrees of freedom in both the LT and HT phases should render the two phases more compatible, reducing the activation energy barrier for nucleation of a more ordered bilayer phase during cooling—or compression—and lowering both the isobaric and isothermal hysteresis²⁹.

In addition to its influence on operating pressure, hysteresis adversely impacts the second-law efficiency and coefficient of performance (COP) of any caloric cooling cycle because of dissipative heat losses^{14,15}. The impact of hysteresis on efficiency can be quantified by calculating an idealized thermodynamic efficiency, η —relative to the Carnot efficiency—with a simple material model that accounts for dissipative losses due to hysteresis in a Carnot-like cycle¹⁴:

$$\eta = \frac{\text{COP}}{\text{COP}_{\text{Carnot}}} = \frac{1}{1 + 4 \frac{\Delta T_{\text{hys}}}{\Delta T_{\text{ad,max}}}}$$

Based on this model, caloric materials with $\Delta T_{\text{hys}}/\Delta T_{\text{ad,max}}$ of less than 10% will have idealized second-law efficiencies competitive with those of conventional vapor compression-based systems

245 (~85%)³⁰. Excitingly, (DA)₂MnCl₄ and (NA)₂CuBr₄ have the potential to reach the second-law efficiencies of 89 and 92%, respectively, based on their intrinsic barocaloric properties.

Overall, these results highlight exciting opportunities to exploit the tunability of 2-D perovskites to independently manipulate the phase-change hysteresis, entropy, and sensitivity to pressure of chain-melting transitions for improved barocaloric performance. For instance, it should
250 be possible to realize phase transitions with even higher entropy changes through functionalization of the organic bilayers—such as by introducing hydrogen bond donor–acceptor pairs^{31,32}—and even lower hysteresis through modification of the organic–inorganic interface—such as by incorporating mixtures of different halide anions or introducing defects. In addition, the anisotropic nature of the chain-melting transition in (DA)₂MnCl₄ and (NA)₂CuBr₄ suggests that
255 uniaxial stress, which can be readily applied through mechanical actuation, may be able to drive large elastocaloric effects in 2-D perovskites. More broadly, solid-state chain-melting transitions are not unique to 2-D perovskites, and many other classes of layered materials—including di-*n*-alkylammonium salts³³, alkylammonium-modified layered silicates³⁴, and metal-alkylphosphonate salts³⁵—undergo reversible phase transitions near ambient temperature
260 that should produce colossal barocaloric effects and have yet to be explored.

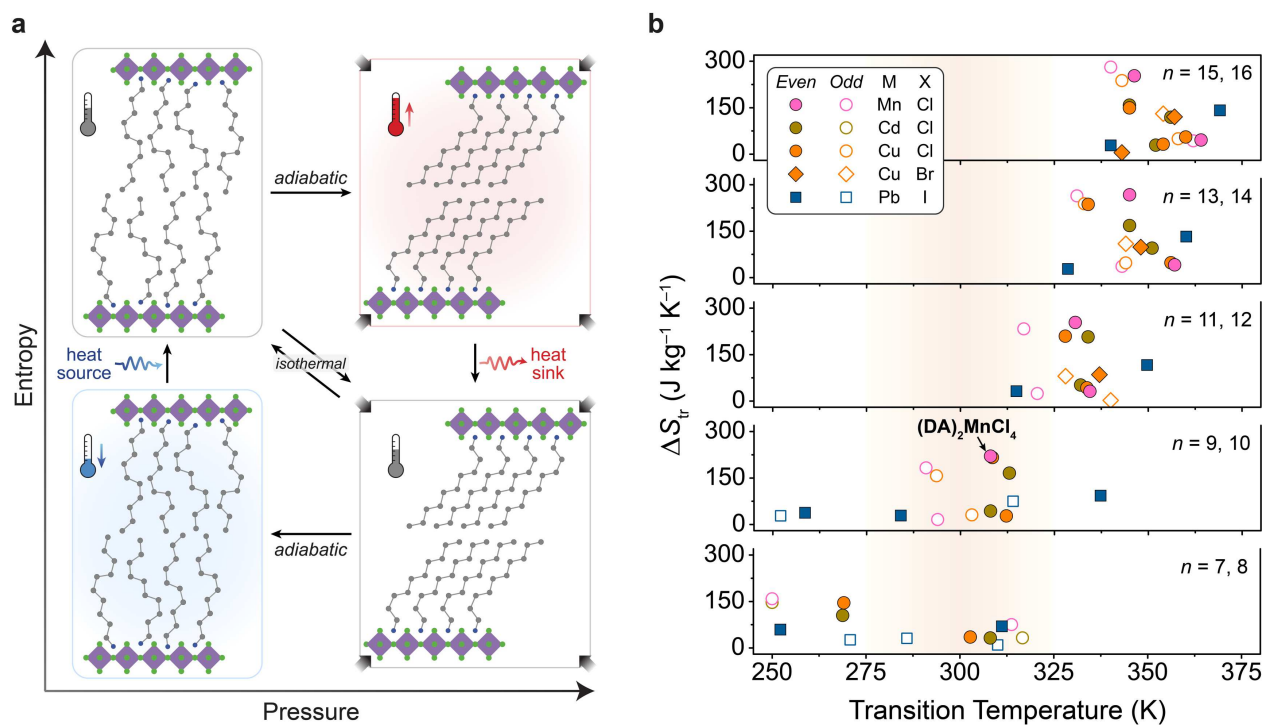


Fig. 1 | Barocaloric cooling with two-dimensional (2-D) metal-halide perovskites. **a**, Illustration of how the pressure-dependence of chain-melting transitions in the organic bilayers of hybrid 2-D perovskites can be leveraged to drive a barocaloric cooling cycle. Each cooling cycle begins with an adiabatic (Brayton-like cycle) or isothermal (Stirling-like cycle) increase in pressure that induces a 1st order phase transition from an expanded, high-entropy phase of the 2-D perovskite to a contracted, low-entropy phase. Heat released during this exothermic transition is dissipated to a heat sink, returning the material to its original temperature but now at a lower entropy. The pressure is then adiabatically or isothermally decreased to reverse the phase transition and cool a heat source. **b**, Comparison of phase transition entropies, ΔS_{tr} , and transition temperatures, T_{tr} , for chain-melting transitions in select 2-D perovskites of the form $(C_nH_{2n+1}NH_3)_2MX_4$ ($n = 7-16$; M = Mn, Cd, Cu, or Pb; X = Cl, Br, or I). Thermally induced phase transitions in 2-D perovskites are often accompanied by large changes in entropy that are sensitive to the length of the hydrocarbon chain and the identity of metal and halide in the inorganic layer. Many of these chain-melting transitions involve one or more minor transitions that occur at lower or higher temperatures than the major transition, but (DA) (DA = decylammonium) features a single chain-melting transition with a large entropy change near ambient temperature.

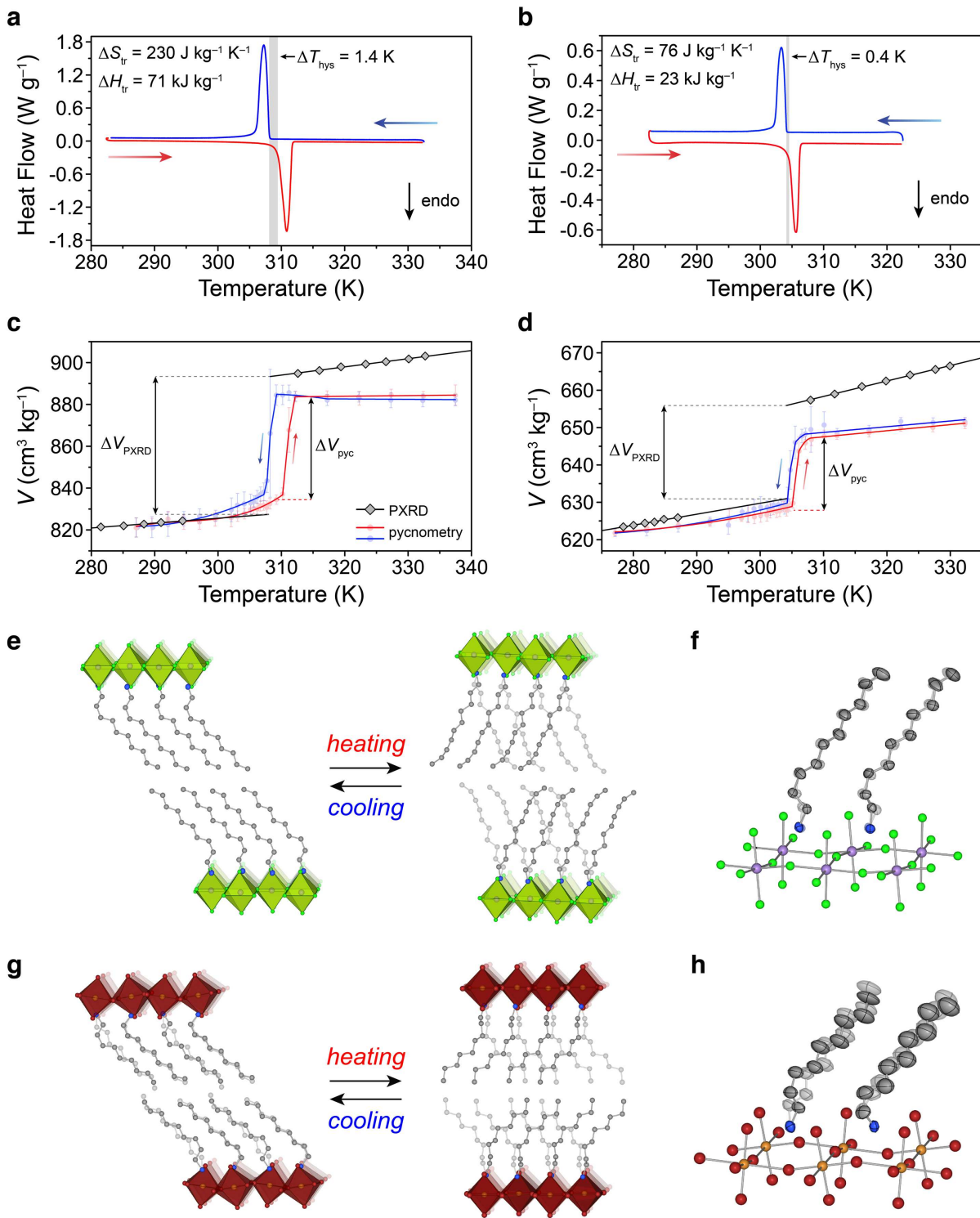


Fig. 2 | Thermally induced chain-melting transitions in $(DA)_2MnCl_4$ and $(NA)_2CuBr_4$ at ambient pressure.
a, b, Differential scanning calorimetry (DSC) traces for **(a)** $(DA)_2MnCl_4$ and **(b)** $(NA)_2CuBr_4$ at 1 bar with heating (red) and cooling (blue) rates of $2\ K\ min^{-1}$. Thermal hysteresis (ΔT_{hys}) is indicated by the vertical grey bars. Note that ΔT_{hys} is calculated as the difference between heating and cooling transition onset temperatures, with $\Delta T_{hys} = T_{tr, heating} - T_{tr, cooling}$. **c, d,** Specific volumes obtained from variable-temperature powder X-ray diffraction and He pycnometry measurements are used to determine the volume changes, ΔV , that accompany the chain-melting transition for **(c)** $(DA)_2MnCl_4$ and **(d)** $(NA)_2CuBr_4$. **e-h,** Variable-temperature crystal structures of the

low-temperature (LT) and high-temperature (HT) phases of **(e)** $(\text{DA})_2\text{MnCl}_4$ and **(g)** $(\text{NA})_2\text{CuBr}_4$. Note that the LT crystal structures were both obtained at 270 K, while the HT crystal structures were obtained at 330 K and 335 K for $(\text{DA})_2\text{MnCl}_4$ and $(\text{NA})_2\text{CuBr}_4$, respectively. The conformations of the alkylammonium chains in the LT phases are shown for **(f)** $(\text{DA})_2\text{MnCl}_4$ and **(h)** $(\text{NA})_2\text{CuBr}_4$ with atomic displacement parameters at 50% probability for the C and N atoms of the alkylammonium chains. Purple, orange, green, brown, grey, and blue spheres represent Mn, Cu, Cl, Br, C, and N atoms, respectively. H atoms are omitted for clarity. Note that DA chains are disordered over a special position in both the LT and HT phases, while NA chains are modeled with two-part disorder in the LT phase and disordered over a special position in the HT phase.

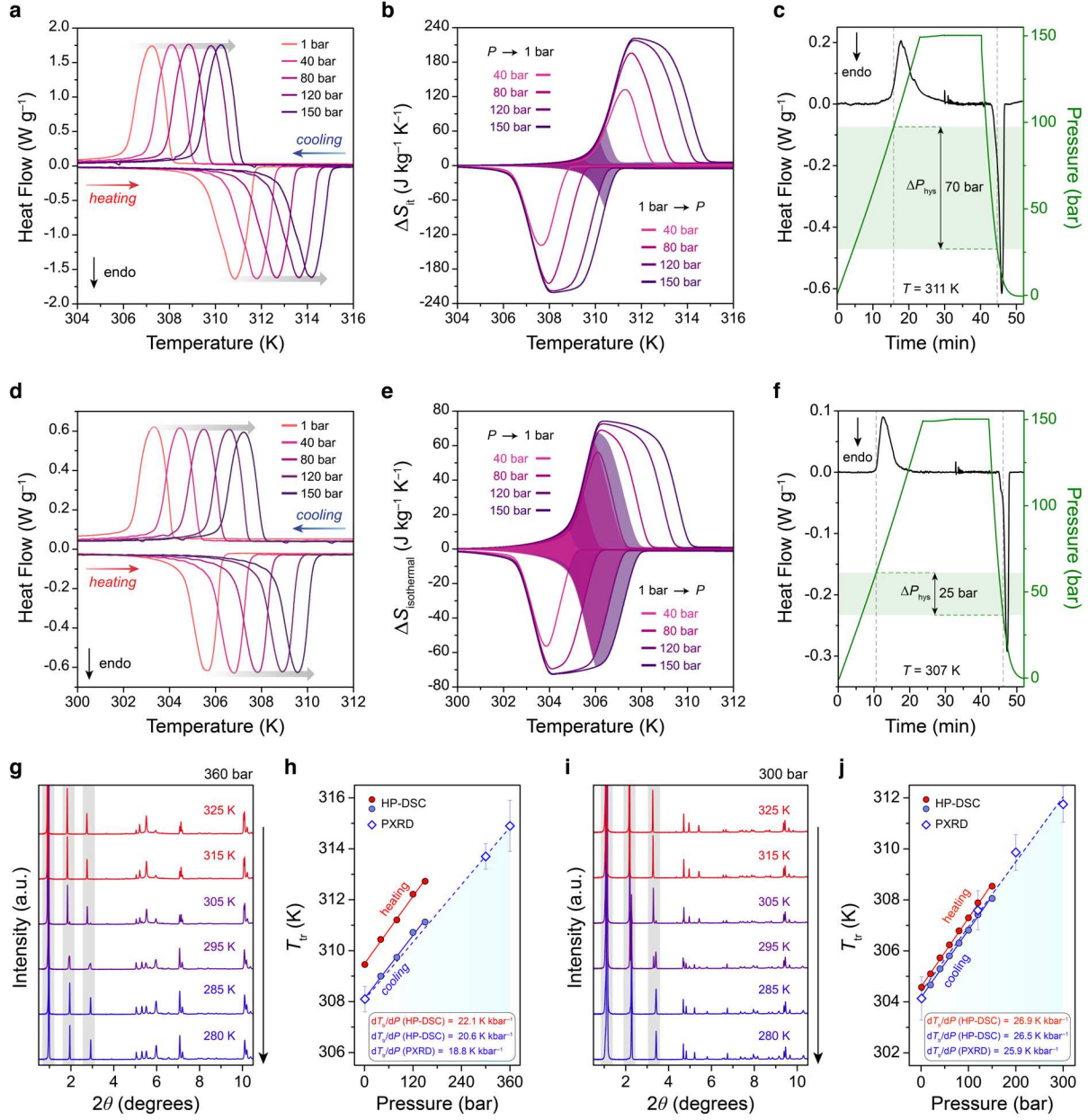


Fig. 3 | Barocaloric effects in 2-D metal-halide perovskites. **a, d**, DSC measurements under applied hydrostatic pressure for **(a)** $(\text{DA})_2\text{MnCl}_4$ and **(d)** $(\text{NA})_2\text{CuBr}_4$ with heating and cooling rates of 2 K min^{-1} . **b, e**, Isothermal entropy changes, ΔS_{it} , are calculated by the quasi-direct method for **(b)** $(\text{DA})_2\text{MnCl}_4$ and **(e)** $(\text{NA})_2\text{CuBr}_4$ for compression from ambient pressure and for decompression to ambient pressure. The shaded area indicates the reversible ΔS_{it} within this pressure range. **c, f**, Direct evaluation of pressure hysteresis, ΔP_{hys} , through quasi-isothermal DSC experiments for **(c)** $(\text{DA})_2\text{MnCl}_4$ and **(f)** $(\text{NA})_2\text{CuBr}_4$ at 311 K and 307 K, respectively, with pressure cycling from 1 to 150 bar. ΔP_{hys} is calculated as the difference between the onset pressure for the compression-induced exotherm and the decompression-induced endotherm and is indicated by the horizontal green bar. **g, i**, Variable-temperature powder X-ray diffraction (PXR) patterns for **(g)** $(\text{DA})_2\text{MnCl}_4$ and **(i)** $(\text{NA})_2\text{CuBr}_4$ at 360 bar and 300 bar of He, respectively, while cooling from 325 K to 280 K, with an X-ray wavelength of 0.45237 \AA . **h, j**, The pressure dependence of the chain-melting transition temperature as determined by HP-DSC (circles) and PXR (diamonds) is used to calculate the barocaloric coefficient, dT_{tr}/dP , for **(h)** $(\text{DA})_2\text{MnCl}_4$ and **(j)** $(\text{NA})_2\text{CuBr}_4$. Red and blue symbols indicate the phase transition temperatures during heating and cooling, respectively.

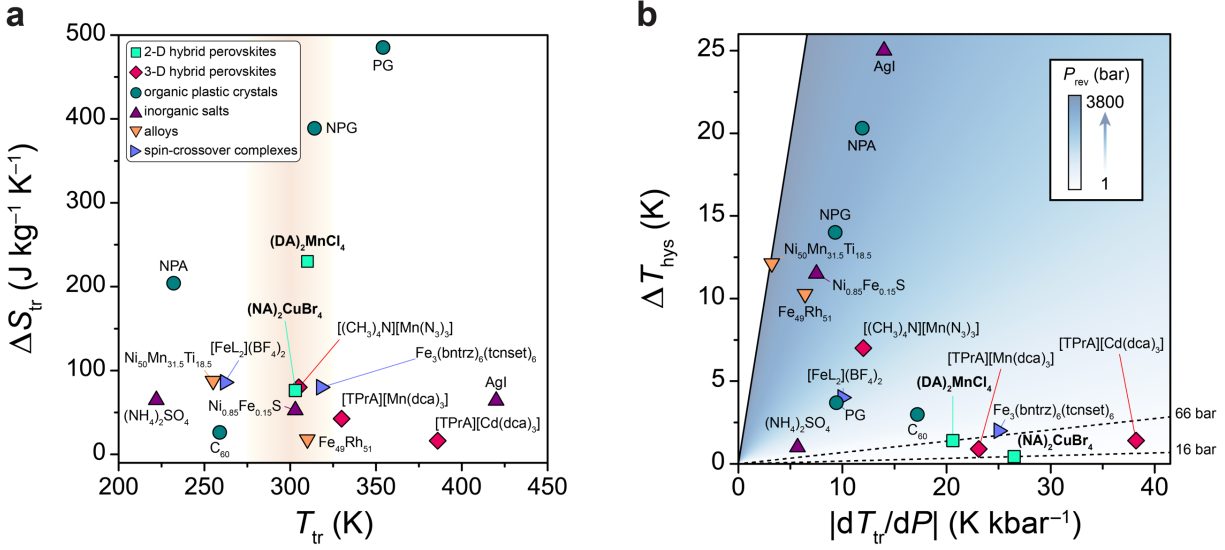


Fig. 4 | Properties of representative barocaloric materials. **a**, Comparison of the phase-change entropy, ΔS_{tr} , and temperature, T_{tr} , for different classes of barocaloric materials. Note that ΔS_{tr} and T_{tr} are shown for endothermic transitions, and ΔS_{tr} represents the maximum isothermal entropy change that could be driven by the pressure-induced phase transition. **b**, Comparison of thermal hysteresis, ΔT_{hys} , and barocaloric coefficient, dT_{tr}/dP , for leading barocaloric materials, with dT_{tr}/dP values corresponding to exothermic transitions for materials that exhibit conventional barocaloric effects and endothermic transitions for materials that exhibit inverse barocaloric effects. The minimum pressure required to achieve a reversible entropy change, P_{rev} , is calculated as $P_{rev} = \Delta T_{hys} / |dT_{tr}/dP|$, and indicated by shading from blue (high P_{rev}) to white (low P_{rev}). A comprehensive tabulation of barocaloric properties, including reversible and irreversible ΔS_{it} values, is provided in Extended Data Tables 1 and 2.

1. Dupont, J. L., Domanski, P., Lebrun, P. & Ziegler, F. *The Role of Refrigeration in the Global Economy*. 38th Note on Refrigeration Technologies (International Institute of Refrigeration). (2019).
2. Coulomb, D., Dupont, J.-L. & Morlet, V. *The Impact of the Refrigeration Sector on Climate Change*. 35th Note on Refrigeration Technologies (International Institute of Refrigeration). (2017).
3. International Energy Agency, *The future of cooling: Opportunities for energy efficient air conditioning*. (2018).
4. Mañosa, L. & Planes, A. Solid-state cooling by stress: A perspective. *Appl. Phys. Lett.* **116**, 050501 (2020).
5. Cazorla, C. Novel mechanocaloric materials for solid-state cooling applications. *Appl. Phys. Rev.* **6**, 041316 (2019).
6. Moya, X. & Mathur, N. D. Caloric materials for cooling and heating. *Science* **370**, 797–803 (2020).
7. U.S. Department of Energy, Office of Energy Efficiency and Renewable Energy, *Energy Savings Potential and RD&D Opportunities for Commercial Building HVAC Systems*. (2017).
8. Takeuchi, I. & Sandeman, K. Solid-state cooling with caloric materials. *Phys. Today* **68**, 48–54 (2015).
9. Aznar, A. *et al.* Reversible and irreversible colossal barocaloric effects in plastic crystals. *J. Mater. Chem. A* **8**, 639–647 (2019).
10. Li, B. *et al.* Colossal barocaloric effects in plastic crystals. *Nature* **567**, 506–510 (2019).
11. Lloveras, P. *et al.* Colossal barocaloric effects near room temperature in plastic crystals of neopentylglycol. *Nat. Commun.* **10**, 1803 (2019).
12. Gutfleisch, O. *et al.* Mastering hysteresis in magnetocaloric materials. *Philos. Trans. R. Soc. A* **374**, 20150308 (2016).
13. Brown, T. D., Buffington, T. & Shamberger, P. J. Effects of hysteresis and Brayton cycle constraints on magnetocaloric refrigerant performance. *J. Appl. Phys.* **123**, 185101 (2018).
14. Hess, T. *et al.* Thermal hysteresis and its impact on the efficiency of first-order caloric materials. *J. Appl. Phys.* **127**, 075103 (2020).
15. Masche, M., Ianniciello, L., Tušek, J. & Engelbrecht, K. Impact of hysteresis on caloric cooling performance. *Int. J. Refrig.* **121**, 302–312 (2021).
16. Domalski, E. S. & Hearing, E. D. Heat capacities and entropies of organic compounds in the condensed phase. Volume III. *J. Phys. Chem. Ref. Data* **25**, 1–525 (1996).
17. McLinden, M. O. *Thermophysical properties of refrigerants*. *ASHRAE Handbook: Fundamentals*. (ASHRAE, 2009).
18. Turturro, A. & Bianchi, U. Conformational contribution to the entropy of melting. I. Linear chain hydrocarbons. *J. Chem. Phys.* **62**, 1668–1673 (1975).
19. Sharma, A., Tyagi, V. V., Chen, C. R. & Buddhi, D. Review on thermal energy storage with phase change materials and applications. *Renew. Sustain. Energy Rev.* **13**, 318–345 (2009).
20. Busico, V., Carfagna, C., Salerno, V., Vacatello, M. & Fittipaldi, F. The layer perovskites as thermal energy storage systems. *Sol. Energy* **24**, 575–579 (1980).

21. Mitzi, D. B. Synthesis, Structure, and Properties of Organic-Inorganic Perovskites and Related Materials. in *Prog. Inorg. Chem: Volume 48*. 1–121 (Wiley, 1999).
22. Ciajolo, M. R., Corradini, P. & Pavone, V. Comparative studies of layer structures: The crystal structure of bis(monodecylammonium)tetrachloromanganate(II). *Gazz. Chim. Ital.* **106**, 807 (1976).
23. Guillaume, F. *et al.* Molecular motions of decylammonium chains in the perovskite type layered compound (C₁₀H₂₁NH₃)₂MnCl₄. *Mol. Phys.* **67**, 665–679 (1989).
24. Kind, R. *et al.* Dynamics of the *n*-decylammonium chains in the perovskite-type layer structure compound (C₁₀H₂₁NH₃)₂CdCl₄. *J. Chem. Phys.* **71**, 2118–2130 (1979).
25. Samara, G. A. *et al.* Effects of pressure and ambient species on the orientational ordering in solid C₆₀. *Phys. Rev. B* **47**, 4756–4764 (1993).
26. Moya, X., Kar-Narayan, S. & Mathur, N. D. Caloric materials near ferroic phase transitions. *Nat. Mater.* **13**, 439–450 (2014).
27. Gorev, M. V., Bogdanov, E. V. & Flerov, I. N. *T*-*p* phase diagrams and the barocaloric effect in materials with successive phase transitions. *J. Phys. D: Appl. Phys.* **50**, 384002 (2017).
28. Fultz, B. *Phase Transitions in Materials*. (Cambridge University Press, 2014).
29. James, R. D. & Zhang, Z. A Way to Search for Multiferroic Materials with “Unlikely” Combinations of Physical Properties. in *Magnetism and Structure in Functional Materials*. 159–175 (Springer, 2005).
30. Domanski, P. A., Steven Brown, J., Heo, J., Wojtusiak, J. & McLinden, M. O. A thermodynamic analysis of refrigerants: Performance limits of the vapor compression cycle. *Int. J. Refrig.* **38**, 71–79 (2014).
31. Li, X., Hoffman, J. M. & Kanatzidis, M. G. The 2D halide perovskite rulebook: How the spacer influences everything from the structure to optoelectronic device efficiency. *Chem. Rev.* **121**, 2230–2291 (2021).
32. Smith, I. C., Smith, M. D., Jaffe, A., Lin, Y. & Karunadasa, H. I. Between the sheets: postsynthetic transformations in hybrid perovskites. *Chem. Mater.* **29**, 1868–1884 (2017).
33. Steinert, S., Voigt, W., Glausch, R. & Neuschütz, M. Thermal characteristics of solid–solid phase transitions in long-chain dialkyl ammonium salts. *Thermochim. Acta* **435**, 28–33 (2005).
34. Osman, M. A., Ploetze, M. & Skrabal, P. Structure and properties of alkylammonium monolayers self-assembled on montmorillonite platelets. *J. Phys. Chem. B* **108**, 2580–2588 (2004).
35. Almeida, O. J. & Dixon, B. G. Lamellar metallo-alkylphosphonates as solid-state phase-change materials. *Chem. Mater.* **7**, 2039–2044 (1995).

Supporting Information is linked to the online version of the paper at www.nature.com/nature.

Acknowledgments This research was partially supported by the Climate Change Solutions Fund at Harvard University and by the Arnold and Mabel Beckman Foundation through a Beckman Young Investigator grant awarded to J.A.M. and a Beckman Postdoctoral Fellowship to A.H.S. We also thank the Korea Foundation for Advanced Studies for a graduate fellowship awarded to J.S. X-ray diffraction data were collected on beamline 17-BM at the Advanced Photon Source at Argonne National Laboratory, which is supported by the U.S. Department of Energy, Office of Science, Office of Basic Energy Sciences under Contract No. DE-AC02-06CH11357. We thank Dr. Marc-Antoine Thermitus, Dr. Stefan Schmölder, and Dr. Steve Sauerbrunn for helpful discussions on high-pressure calorimetry experiments. The authors also thank Malia Wenny and Rahil Ukani for helpful discussions.

Author contributions J.S. and J.A.M. formulated the project. J.S. synthesized the compounds. J.S., R.D.M., A.H.S., S.Z., and A.Y.A. collected and analyzed the powder X-ray diffraction data. J.S., R.D.M., A.H.S., and S.-L.Z. collected and analyzed single-crystal X-ray diffraction data. J.S. collected and analyzed the high-pressure calorimetry data. J.S. and J.A.M. wrote the paper, and all authors contributed to revising the paper.

Competing interests J.S. and J.A.M. are inventors on a patent application related to this work held and submitted by Harvard University that covers barocaloric properties of two-dimensional perovskites and related compounds.

Data and materials availability The supplementary materials contain complete experimental details for all compounds reported herein. Crystallographic data have been made available free of charge from the Cambridge Crystallographic Data Centre under reference numbers CCDC 2075108–2075113.

Methods

Materials

All compounds were synthesized and handled in air unless otherwise noted. Anhydrous diethyl ether was obtained from a Pure Process Technology anhydrous solvent system. Anhydrous methanol and ethanol were purchased from a commercial vendor and used as received. All other reagents were purchased from commercial vendors and used as received.

Synthesis of (DA)₂MnCl₄ (DA = decylammonium, C₁₀H₂₁NH₃)

Decylamine ($\geq 99.0\%$ purity) and hydrochloric acid (HCl, 37 wt %) were purchased from Sigma Aldrich and used without further purification. Decylammonium chloride (C₁₀H₂₁NH₃Cl, (DA)Cl) was first synthesized by adding HCl (550 μ L, 6.6 mmol) into a solution of decylamine (1.1 mL, 5.5 mmol) in ca. 5 mL ethanol in an ice water bath with stirring. After evaporating the solvent under reduced pressure, the resulting white powder of (DA)Cl was washed with diethyl ether and dried under vacuum at room temperature for 1 day. Crystalline powders of (DA)₂MnCl₄ were prepared in a similar manner to previously reported syntheses^{22,36}. Specifically, (DA)Cl (96.9 mg, 0.5 mmol) was first dissolved in 4.0 mL of ethanol. After several minutes of stirring, MnCl₂·4H₂O (49.5 mg, 0.25 mmol) was added to the solution, and the solution was heated to 65 °C. Pale-pink crystals were obtained upon cooling the resulting solution to room temperature at a rate of 4 K h⁻¹. The crystals were filtered, washed with diethyl ether (5 \times 10 mL), and dried under vacuum for 6 h to afford 45.2 mg (35.2% yield) of product. Single crystals suitable for X-ray structure determination were obtained by cooling at a rate of 2 K h⁻¹.

Synthesis of (NA)₂CuBr₄ (NA = decylammonium, C₉H₁₉NH₃)

Nonylamine ($\geq 99.5\%$ purity) and hydrobromic acid (HBr, 48 wt %) were purchased from Sigma Aldrich and used without further purification. Nonylammonium bromide (C₉H₁₉NH₃Br, (NA)Br) was first synthesized by adding HBr (545 μ L, 4.8 mmol) into a solution of nonylamine (733 μ L, 4.0 mmol) in ca. 5 mL ethanol in an ice water bath with stirring. After evaporating the solvent under reduced pressure, the resulting white powder of (NA)Br was washed with diethyl ether and dried under vacuum at room temperature for 1 day. Crystalline powders of (NA)₂CuBr₄ were prepared by dissolving of CuBr₂ (402 mg, 1.8 mmol) and (NA)Br (807 mg, 3.6 mol) in 2 mL of ethanol at 65 °C. The solution was slowly cooled to room temperature at a rate of 4 K h⁻¹ and then further cooled to 5 °C for 1 h. The resulting dark purple precipitate was filtered, washed with diethyl ether (5 \times 10 mL), and dried under vacuum for 12 h to afford 705 mg (58.3% yield) of product. Single crystals suitable for X-ray structure determination were obtained by slow evaporation of a 1-mL solution of (NA)₂CuBr₄ (202 mg, 0.3 mmol) in methanol. Anal. Calcd. for (C₉H₁₉NH₃)₂CuBr₄: C: 32.19%, H: 6.60%, N: 4.17%, Br: 47.58%. Found: C: 31.84%, H: 6.69%, N: 4.43%, Br: 47.76%.

Thermogravimetric analysis

Samples were loaded into a TGA 550 from TA Instruments in open aluminum pans with a stainless-steel bail under air and heated at a rate of 4 K min⁻¹ from ambient to 500 °C under a 10 mL min⁻¹ N₂ flow with an empty aluminum pan/stainless steel bail used as a reference counterweight. The TGA mass was calibrated using a series of 3 reference masses, while the TGA temperature was calibrated to the Curie temperature of nickel. The thermogravimetric analyses of (DA)₂MnCl₄ and (NA)₂CuBr₄ are shown in Supplementary Fig. 1, and both compounds are stable until over 100 °C.

High-pressure differential scanning calorimetry (HP-DSC)

DSC measurements over the pressure range from 1 to 150 bar were carried out in a Netzsch high-pressure DSC (DSC 204 HP Phoenix) equipped with a liquid nitrogen cooling system. The DSC sample cell is surrounded by an autoclave, where the internal pressure and gas flow are regulated by an electronic pressure control device. The autoclave is connected to a circulating water bath that provides an additional source of external temperature control during experiments. Temperature and heat flow signals were calibrated at each measured pressure using an indium standard³⁷. Helium gas (ultra-high purity, 99.999%) was used as a pressure-transmitting medium. All DSC samples were prepared in air using 5–10 mg of sample and were sealed in aluminum pans with a pierced lid. An empty, aluminum pan with a pierced lid was used as a reference. All measurements were carried out under flowing gas with a He flow rate of 50 mL min⁻¹. Unless otherwise noted, heating and cooling rates of 2 K min⁻¹ were used for isobaric measurements. Full HP-DSC traces for (DA)₂MnCl₄ and (NA)₂CuBr₄ are shown in Supplementary Figs. 2 and 3, respectively.

Determination of T_{tr} , ΔH_{tr} , and ΔS_{tr}

Phase transition temperatures, T_{tr} , and enthalpies, ΔH_{tr} , were determined using the TRIOS software from TA Instruments. Peaks were selected for analysis by defining a temperature range containing the peak of interest. The lower and upper bounds of the temperature range were chosen to encompass the phase transition, which starts with a deviation from the baseline and ends with a return to baseline. Prior to determination of T_{tr} or ΔH_{tr} , a baseline, which models the heat flow in the absence of a phase transition, must be generated to approximate the baseline in the transition region. Baselines were generated within the defined temperature range to determine the slope of the lower and higher temperature limits and shape of the baseline. Baselines were generated using mutual tangent slopes before and after the transition peak with a sigmoidal baseline, which we found to produce the most physically reasonable baselines.

The extrapolated onset temperature was reported as the transition temperature, as is standard in DSC data analysis, because the onset temperature—unlike the peak temperature—is relatively independent of experimental parameters like heating rate or sample mass. The onset temperature was determined by identifying the region of the onset transition peak that has the steepest slope, defining a tangent to that region, and then extending the tangent to the generated baseline. The intersection between the baseline and the tangent is reported as T_{tr} . Transition peaks were integrated between the upper and lower temperature limits with the baseline subtracted to provide ΔH_{tr} , and phase transition entropies, ΔS_{tr} , were calculated as $\Delta S_{tr} = \Delta H_{tr}/T_{tr}$. If physically reasonable limits were chosen, T_{tr} and ΔH_{tr} did not depend strongly on the choice of the temperature limits, and such variations were within the error of the measurements, which is estimated to be ± 0.04 °C for T_{tr} and $< 3\%$ for ΔH_{tr} based on repeated measurements of the melting transition of an indium standard.

Evaluation of isobaric and isothermal entropy change

Isobaric entropy changes, ΔS_{ib} , were calculated as a function of temperature and pressure by integrating the HP-DSC heat flow signal Q , obtained at a scan rate of \dot{T} near the transition peak over the temperature range from T_i to T_f after baseline subtraction^{26,38}:

$$\Delta S_{ib}(P, T) = \int_{T_i}^{T_f} \frac{1}{T} \frac{Q(P, T)}{\dot{T}} dT \quad (1)$$

In a typical isobaric measurement with a scan rate of 2 K min^{-1} , the temperature range for peak integration, $T_f - T_i$, was set to 16 K for consistency, with $T_i = T_{tr} - 8 \text{ K}$ and $T_f = T_{tr} + 8 \text{ K}$. Note that there are not any noticeable changes in the HP-DSC heat flow peak shapes or widths up to at least 150 bar. Baselines for peak integration were generated using mutual tangent slopes, and the tangents before and after the transition peak were created from $T_i - 4 \text{ K}$ to T_i and from T_f to $T_f + 4 \text{ K}$, respectively. Tangent slopes were created over this extended temperature range to minimize any uncertainty in integration, particularly at higher gas pressures which lead to more noisy baselines. Pressure-induced isothermal entropy changes, ΔS_{it} , were then calculated by the quasi-direct method²⁶ as the difference between ΔS_{ib} at ambient pressure, $\Delta S_{ib}(1 \text{ bar}, T)$, and ΔS_{ib} at elevated pressure, $\Delta S_{ib}(P, T)$. For ΔS_{it} corresponding to the endothermic, disordering transition induced by decompression ($P \rightarrow 1 \text{ bar}$), ΔS_{ib} values were obtained from heating data:

$$\Delta S_{it}(P \rightarrow 1 \text{ bar}) = \Delta S_{ib, \text{heating}}(1 \text{ bar}, T) - \Delta S_{ib, \text{heating}}(P, T) \quad (2)$$

For ΔS_{it} corresponding to the exothermic, ordering transition induced by compression ($1 \text{ bar} \rightarrow P$), ΔS_{ib} values were obtained from cooling data:

$$\Delta S_{it}(1 \text{ bar} \rightarrow P) = \Delta S_{ib, \text{cooling}}(P, T) - \Delta S_{ib, \text{cooling}}(1 \text{ bar}, T) \quad (3)$$

The reversible values of ΔS_{it} were estimated from the overlap between compression-induced and decompression-induced ΔS_{it} curves reflected across the temperature axis. The isobaric and isothermal entropy curves of $(\text{DA})_2\text{MnCl}_4$ and $(\text{NA})_2\text{CuBr}_4$ are shown in Supplementary Figs. 4 and 5, and the pressure dependence of the reversible isothermal entropy changes for both compounds is shown in Extended Data Fig. 1.

Since the integration was carried out near the transition without taking into account the heat capacity of each phase, the isobaric entropy curves are flat before and after the phase transition region. Incorporating the heat capacity of each phase would introduce a positive slope in the isobaric entropy curves before and after the transition. However, we note that accounting for the heat capacities would have a negligible effect on the overall evaluation of the isothermal entropy changes near the phase transition over this pressure range.

Evaluation of additional entropy changes, ΔS_+ , outside of the first-order phase transition

Pressure-induced changes in isothermal entropy can also arise outside of the phase transition region. This entropy contribution, ΔS_+ , is often referred to as the elastic heating contribution^{6,39} and can be calculated using the following formula derived from the Maxwell relation $(\partial V/\partial T)_P = -(\partial S/\partial P)_T$:

$$\Delta S_+ (P_f - P_i) = - \int_{P_i}^{P_f} \left(\frac{\partial V}{\partial T} \right) dP \quad (4)$$

For normal barocaloric materials with $(\partial V/\partial T)_P > 0$, this entropy contribution originates from the applied pressure counteracting entropy increases due to thermal fluctuations. By assuming that the thermal expansion coefficient is independent of pressure, ΔS_+ can be estimated as

$$\Delta S_+ = -[(\partial V/\partial T)_{P=0}] \Delta P = -(V \cdot \alpha) \cdot \Delta P \quad (5)$$

where V , ΔP , and α denote the specific volume, driving pressure $\Delta P = P_f - P_i$, and thermal expansion coefficient at ambient pressure, respectively, with $\alpha = V^{-1}(\partial V/\partial T)_{P=0}$. Note that the direct calculation of ΔS_+ requires high-pressure heat capacity data, but Eqn. 5 is commonly used to estimate ΔS_+ since high-pressure heat capacity measurements are difficult to perform accurately.

Although both $(\text{DA})_2\text{MnCl}_4$ and $(\text{NA})_2\text{CuBr}_4$ display thermal expansion coefficients on the order of 10^{-4} K^{-1} (Supplementary Table 6), their estimated ΔS_+ values are small relative to their transition entropies over the investigated pressure range. For example, for a driving pressure from 1 to 150 bar, ΔS_+ in the LT phases of $(\text{DA})_2\text{MnCl}_4$ and $(\text{NA})_2\text{CuBr}_4$ is predicted to be just $3 \text{ J kg}^{-1} \text{ K}^{-1}$ and $4 \text{ J kg}^{-1} \text{ K}^{-1}$, respectively, while ΔS_+ in the HT phases of $(\text{DA})_2\text{MnCl}_4$ and $(\text{NA})_2\text{CuBr}_4$ is predicted to be $6 \text{ J kg}^{-1} \text{ K}^{-1}$ for both compounds. As such, we did not include contributions from ΔS_+ in our quasi-direct analysis. We note, however, that ΔS_+ can become significant at higher driving pressures and can further enhance the barocaloric effect. In particular, accounting for ΔS_+ would lead to a downward shift in the high-pressure isobaric entropy curves of the LT phase, which would increase the ΔS_{it} values determined from the quasi-direct method. This additional contribution to ΔS_{it} would be expected to reach 10% of ΔS_{tr} at a 1,000 bar driving pressure for $(\text{DA})_2\text{MnCl}_4$ and a 300 bar driving pressure for $(\text{NA})_2\text{CuBr}_4$.

Quasi-isothermal HP-DSC

During the quasi-isothermal pressure cycling experiments, heat flow signals were measured as a function of time while applying or removing a hydrostatic pressure of 150 bar. The temperature was held at 311 K for $(\text{DA})_2\text{MnCl}_4$ and 307 K for $(\text{NA})_2\text{CuBr}_4$. The pressure was increased linearly at a rate of 6 bar min^{-1} and decreased asymptotically at an average rate of 13 bar min^{-1} . To distinguish heat flow signals associated with the pressure-induced phase transitions of each compound from those associated with compression and decompression of He gas, 5 mg of $(\text{C}_{12}\text{H}_{25}\text{NH}_3)_2\text{MnCl}_4$, which was prepared according to a previously reported procedure⁴⁰, was used as a control sample because it does not undergo any phase transitions until above 330 K, well above the transition temperatures for $(\text{DA})_2\text{MnCl}_4$ and $(\text{NA})_2\text{CuBr}_4$. The heat flow signals measured during pressure cycling $(\text{C}_{12}\text{H}_{25}\text{NH}_3)_2\text{MnCl}_4$ at 311 K and 307 K were modeled as a baseline and subtracted from the raw sample data for $(\text{DA})_2\text{MnCl}_4$ and $(\text{NA})_2\text{CuBr}_4$, respectively, to yield pressure-induced heat flow signals as a function of time (Extended Data Fig. 2). Similar to the determination of the transition temperature, T_{tr} , the extrapolated onset pressures were defined

as the transition pressure for pressure-induced endotherms and exotherms. Specifically, the onset pressure was determined by first generating baselines using mutual tangent slopes before and after the pressure-induced transition peak, with the intersection between the baseline and the tangent of the peak representing the onset point. The corresponding pressure at the onset time is reported as the phase transition pressure, and the pressure hysteresis is calculated as the difference between the phase transition pressures during compression and decompression.

During pressure cycling, quasi-isothermal conditions were maintained by adjusting the set temperature of the circulating water bath surrounding the autoclave to compensate for small temperature fluctuations induced by gas compression and decompression. Note that external thermal control measures were identical for all three samples (control, $(\text{DA})_2\text{MnCl}_4$, and $(\text{NA})_2\text{CuBr}_4$). Since the rate at which the pressure was decreased was faster than the rate it was increased, decompression resulted in a larger change in temperature (1 K) than compression (< 0.3 K). However, these small temperature changes were quickly recovered, such that the measured sample temperatures near the phase transition onsets were in close proximity during both compression and decompression (< 0.4 K variation). Maintaining isothermal conditions in the HP-DSC becomes challenging once the phase transition is induced because of the large enthalpy changes that accompany the transition. As the HP-DSC works to counteract the temperature increase induced by an exothermic phase transition—and the temperature decrease induced by an endothermic phase transition—to maintain a constant temperature set point, the instrument drives the transitions to completion. As such, we did not integrate the heat flow signals for these experiments and only used this data to determine the onset pressures for transitions during compression and decompression where isothermality was maintained, allowing pressure hysteresis to be directly measured.

Heat capacity measurements

A Discovery 2500 DSC with a RCS 90 cooling system (TA Instruments) was used to measure the heat capacity of $(\text{DA})_2\text{MnCl}_4$ and $(\text{NA})_2\text{CuBr}_4$ using the ASTM Standard E1269. All runs used to calculate heat capacity were performed under the standard manufacturer calibrations. This includes the Tzero calibration, which achieves flat ($< 5 \mu\text{W}$ variation) baselines by calibrating the cell to a heat flow model containing thermal resistance and capacitance terms for the sample and reference sides of the cell. In addition, an indium standard was used to calibrate the temperature and cell constant.

The ASTM E1269 method calculates heat capacity from three separate DSC runs, which are performed sequentially. All three runs were comprised of a temperature ramp (10 K min^{-1}) over the temperature range of interest with 10 min isothermal holds at the minimum and maximum temperatures to stabilize heat flows before and after the temperature ramps. The first run was conducted with empty pans in the sample and reference position of the DSC to establish a baseline in the absence of sample. Though the DSC baseline is calibrated using the Tzero method, that calibration returns a flat baseline of zero heat flow to an empty cell, while the ASTM baseline accounts for asymmetries that may be introduced due to the introduction of pans to the sample and reference position. The second run was conducted with an empty reference pan and a sample pan containing a sapphire disc to calibrate the heat capacity, and the third run was conducted by replacing the sample pan containing the sapphire with a sample pan containing either $(\text{DA})_2\text{MnCl}_4$ or $(\text{NA})_2\text{CuBr}_4$.

All samples of $(\text{DA})_2\text{MnCl}_4$ and $(\text{NA})_2\text{CuBr}_4$ for heat capacity measurements were prepared under an N_2 atmosphere in Tzero aluminum pans and sealed using a Tzero aluminum press. To ensure adequate heat flows and heat capacity signal, 10 mg or more of sample were used for each heat capacity measurement. In addition, the samples were packed into the pan using the Tzero powder preparation kit to improve thermal contact. The ASTM method specifies that the masses of the empty sample and reference pans should be matched, with ASTM recommending ± 0.01 mg variation and TA instruments recommending ± 0.05 mg variation. The DSC 2500, however, accounts for pan mass differences and the resulting heat flows due to the heat capacity of aluminum using the T4P heat flow. Therefore, when using the T4P heat flow, the pan mass matching criterion is not as stringent. Nevertheless, pan masses were selected here to be within ± 0.1 mg, with the total empty pan mass being near 50 mg.

Non-hermetic Tzero pans were used to allow for He gas to be present over the sample to be consistent with high-pressure DSC measurements and because the non-hermetic lids press directly on the sample, improving thermal control. The DSC 2500 also features a robotic autosampler, which precisely and repeatably loads the sample and reference pans into the DSC cell. For all three runs, the reference pan remained in the cell and was not moved, with only the sample pan being exchanged by the autosampler. The cell purge gas was He at a flow rate of 50 mL min^{-1} . Samples were held under He for at least 30 minutes prior to the temperature ramp.

To examine the variability in our measurement and obtain a representative average heat capacity curve, the measurements of $(\text{DA})_2\text{MnCl}_4$ and $(\text{NA})_2\text{CuBr}_4$ were each conducted 8 times. The same reference pan and sapphire pan was used for all measurements, while a new sample pan with new sample was used for each measurement. All $(\text{DA})_2\text{MnCl}_4$ and $(\text{NA})_2\text{CuBr}_4$ heat capacity measurements were conducted between at least 230 and 360 K, and the averaged data is shown in Supplementary Fig. 6. After noticing a low temperature feature in the heat capacity of $(\text{NA})_2\text{CuBr}_4$, several additional runs were conducted down to 190 K, and an additional run of $(\text{DA})_2\text{MnCl}_4$ was also conducted down to 190 K (Extended Data Fig. 6). The ASTM heat capacity was calculated using a feature in the TRIOS software (TA Instruments), which calculates the heat capacity from a set of three ASTM runs (the baseline, sapphire, and sample runs) with each heat capacity calculation representing a unique set of three runs. The heat capacity data was interpolated onto a common temperature axis and averaged at each temperature point to arrive at an average heat capacity curve for $(\text{DA})_2\text{MnCl}_4$ and $(\text{NA})_2\text{CuBr}_4$. The error was also calculated at each temperature point and is based on the ASTM recommendation, which specifies reporting an error of 2.8 times the standard deviation. The average heat capacity across the phase transition, determined from c_p values 15 K below and above the transition temperature of each compound, is $1550 \pm 60 \text{ J kg}^{-1} \text{ K}^{-1}$ for $(\text{DA})_2\text{MnCl}_4$ and $1180 \pm 50 \text{ J kg}^{-1} \text{ K}^{-1}$ for $(\text{NA})_2\text{CuBr}_4$. From these c_p values, a maximum adiabatic temperature change, $\Delta T_{\text{ad, max}}$, of 43 K and 18 K can be estimated from $T_{\text{ad, max}} = T\Delta S_{\text{it}} / c_p$ for $(\text{DA})_2\text{MnCl}_4$ and $(\text{NA})_2\text{CuBr}_4$, respectively (Extended Data Table 2).

Powder X-ray diffraction (PXRD)

Powder X-ray diffraction data for $(\text{DA})_2\text{MnCl}_4$ and $(\text{NA})_2\text{CuBr}_4$ were collected on beamline 17-BM-B at the Advanced Photon Source (APS) at Argonne National Laboratory, with an X-ray wavelength of 0.45237 \AA . For variable temperature and pressure experiments, approximately 10 mg of sample was loaded into a sapphire capillary ($1.52 \text{ mm} \times 1.07 \text{ mm} \times 50.8 \text{ mm}$, Saint-Gobain Crystals). Each capillary was attached to a custom-designed flow cell equipped with a gas valve, which was mounted onto the goniometer head. A syringe pump (Teledyne ISCO D65) was then connected via a $1/16$ " gas line to the flow cell and used to control the hydrostatic pressure of He

gas (ultra-high purity, 99.999%) from 80 to 360 bar. The internal sample temperature was monitored during PXRD experiments via a K-type thermocouple (0.1 K accuracy) that was in thermal contact with the powder sample within the capillary. The sample temperature was controlled by an Oxford Cryostream (Oxford Cryostream 800+).

In a typical isobaric, variable-temperature PXRD experiment, the sapphire capillary was first equilibrated at 370 K for 10–20 minutes and then the Cryostream temperature was decreased from 370 to 250 K at a rate of 6 K min⁻¹, which led to a change in sample temperature from 335 to 275 K at an average rate of ~3 K min⁻¹. During cooling, powder patterns were collected every 10–20 seconds at a temperature interval of ~1 K. Isothermal, variable-pressure experiments were carried out to determine the compressibility of the LT and HT phases of each sample. Prior to each measurement, samples were equilibrated at the set temperature for 20 minutes. Powder patterns were then collected every 5 bar from 80 to 300 bar, equilibrating for 2 min at each pressure.

Diffraction patterns were analyzed using the software TOPAS-Academic. Unit cell parameters of diffraction patterns were determined by using a standard peak search followed by indexing with a single value decomposition approach. A structureless Le Bail refinement was then performed to refine the unit cell parameters. Variable-temperature PXRD data obtained under isobaric conditions are shown in Supplementary Figs. 8, 9, and Extended Data Fig. 3 for (DA)₂MnCl₄ and Supplementary Figs. 10–12 and Extended Data Fig. 4 for (NA)₂CuBr₄. Comparisons with simulated powder patterns are provided in Supplementary Fig. 13. For both compounds, the temperature and pressure dependence of specific volumes, unit cell parameters, and interlayer distances are provided in Supplementary Figs. 14–18. The thermal expansion coefficients, isothermal compressibility, and volume change during transition each compound are tabulated in Supplementary Tables 6 and 7, and unit cell parameters are tabulated in Supplementary Tables 8 and 9.

Determination of T_{tr} from PXRD

Isobaric, variable-temperature experiments were carried out from 80 to 360 bar to determine the phase transition temperature, T_{tr} , for (DA)₂MnCl₄ and (NA)₂CuBr₄. In particular, we evaluated the temperature dependence of the exothermic transition from the high-temperature (HT) to low-temperature (LT) phases during cooling, $T_{tr, cooling}$, because temperature control during cooling was more reliable than during heating. To identify T_{tr} , changes in the high-intensity (00 l) peaks in the low-angle region (< 4°) of the powder patterns were monitored, with a particular focus on the emergence of a higher-angle shoulder on the right side of each peak that indicates the emergence of the smaller unit cell of the LT. Note that the shoulder intensity as small as 2% of the parental peak intensity was discernible. Since the sample temperature was varied continuously—similar to DSC experiments—the onset temperature for the emergence of the LT phase is reported as T_{tr} . More specifically, the transition onset temperature was estimated to be just above the temperature at which the first powder pattern with the shoulder peaks was. This approach enabled the identification of transition temperatures with an estimated accuracy of 1–2 K.

To further improve the accuracy of T_{tr} determination, we used data from the thermocouple embedded in the sample capillary that recorded the sample temperature every 2 sec. During cooling, the thermocouple temperature trace features a peak, which is attributed to the latent heat of the exothermic transition. Despite the seemingly small signal, this feature can be clearly detected by monitoring the change in sample cooling rate over time. Specifically, the phase transition leads to a sudden spike in the first derivative of sample temperature with respect to time. The onset of

the phase transition was assigned to the temperature at which the first local maximum of the cooling rate curve appears, as this feature—which corresponds to the tangent of the onset transition peak—can be reliably identified across all datasets. Additionally, the uncertainty associated with the determination of the transition onset temperature was defined as the full width at half maximum of the cooling rate peak, which ranges from 1 to 2 K. Note that the T_{tr} values were determined using the sample thermocouple temperature data. At ambient pressure, the onset transition temperatures, $T_{tr, cooling}$, determined by these PXRD experiments were in excellent agreement with those determined by DSC, with a difference of less than 0.4 K. Since the goal of these experiments was to determine the pressure dependence of T_{tr} , rather than the absolute values of T_{tr} , the transition temperatures determined via PXRD were calibrated using the $T_{tr, cooling}$ value determined by DSC at ambient pressure for consistency.

Determination of ΔV_{tr} from PXRD

From the temperature dependence of unit cell volumes at ambient pressure, the specific volume change during the chain-melting transition, ΔV_{tr} , was calculated as the difference between the LT and HT phase volume at the transition temperature (T_{tr}), with $\Delta V_{tr} = V_{LT, tr} - V_{HT, tr}$. The volume at T_{tr} for the LT and HT phases was extrapolated from unit cells determined below and above T_{tr} , respectively, using thermal expansion coefficients for each phase determined at ambient pressure. Specific volume changes from 200 to 300 bar were determined using unit cell volumes measured as a function of pressure at constant temperature (273 K for both LT phases, 323 K for the HT phase of $(DA)_2MnCl_4$, and 314 K for the HT phase of $(NA)_2CuBr_4$). Thermal expansion coefficients were assumed to be independent of pressure over this pressure range, and the thermal expansion coefficients determined for each phase at 1 bar were used to extrapolate the isothermal, high-pressure specific volumes to T_{tr} at each pressure.

Helium pycnometry

Sample densities were determined using an InstruQuest μ -ThermoPyc variable temperature He pycnometer. In a typical measurement, ~ 150 mg of sample was transferred to the sample holder, and the sample mass was obtained. The holder was then placed in the instrument test chamber, and the headspace was evacuated and refilled five times with He. The sample was then cycled multiple times through the phase transition with the chamber volume determined every 2–5 °C away from the transition and every 0.5–1.0 °C close to the transition. For a measurement of unknown volume in a sample holder, V_{test} , in the sample chamber with a known volume of V_{sc} , at a temperature T_{sc} , the sample chamber was first pressurized to ~ 200 kPa and the initial pressure (P_i) was measured. A reference chamber of known volume (V_{rc}) was initially equilibrated with ambient pressure (P_a) and temperature (T_{rc}). The sample chamber was then connected to a reference chamber. After equilibration, the final pressure in the combined chamber, P_f , was measured. Since the system is closed when the two chambers are connected, the ideal gas law and conservation of moles can be used to provide the following relationship:

$$\frac{P_i(V_{sc} - V_{test})}{RT_{sc}} + \frac{P_a V_{rc}}{RT_{rc}} = \frac{P_f(V_{sc} - V_{test})}{RT_{sc}} + \frac{P_f V_{rc}}{RT_{rc}} \quad (6)$$

where the left- and right-hand sides denote the moles of gas before and after connecting the sample and reference chamber, respectively.

Solving for V_{test} gives:

$$V_{\text{test}} = V_{\text{sc}} - V_{\text{r}} \left(\frac{T_{\text{s}}}{T_{\text{r}}} \right) \frac{(P_{\text{f}} - P_{\text{a}})}{(P_{\text{i}} - P_{\text{f}})} \quad (7)$$

Since V_{test} includes the volume of the empty sample holder (V_{h}) that had been measured previously, sample volume (V_{sample}) was determined by subtracting V_{h} from V_{test} , with $V_{\text{sample}} = V_{\text{test}} - V_{\text{h}}$. For each volume measurement, the temperature was fully equilibrated until the temperature variation was less than 0.2 °C. At each temperature, the chamber volumes were measured five times to obtain good statistics. Prior to measurement of the sample, a calibration run of the empty sample holder was performed over the same temperature range. The sample mass was redetermined after the measurement and found to have decreased by no more than 0.5 mg. Uncertainties of the reported densities were determined by propagation of the standard deviations of the empty and filled chamber volumes and the sample mass. ΔV_{tr} values for both compounds are summarized in Supplementary Table 10.

X-ray crystallography

X-ray diffraction analyses were performed on single crystals coated with Paratone-N oil and mounted on MiTeGen microloops using Dow Corning high vacuum grease. The temperature during data collection was controlled from 100 to 335 K using an Oxford Cryostreams nitrogen flow apparatus. Crystals were first mounted at 270 K, and 270 K datasets were collected. Crystals were then cooled to 100 K for 100 K data collection. After 100 K datasets, high-temperature datasets were collected: 330 K for (DA)₂MnCl₄ and 335 K for (NA)₂CuBr₄. The temperature was manipulated at a rate of 60 K h⁻¹. The intensities of the reflections were collected by a Bruker D8 diffractometer with CMOS area detector (MoK α radiation, $\lambda = 0.71073$ Å). The collection method involved 0.5° scans in ω at 23° in 2θ with a detector distance of 9 cm for (DA)₂MnCl₄ and 8 cm for (NA)₂CuBr₄. Data integration down to 0.84 Å resolution was carried out using SAINT V8.37A with reflection spot size optimization. Absorption corrections were made with the program SADABS. All single-crystal structures were solved by the Intrinsic Phasing methods and refined by least-squares methods against F^2 using SHELXT-2014 and SHELXL-2018 with the OLEX2 interface. All non-H atoms, including all the disorder atoms, were located in difference-Fourier maps and then refined anisotropically. Hydrogen atoms were placed at idealized positions and refined using a riding model. The isotropic displacement parameters of all hydrogen atoms were constrained to be 1.2 times the parameters of the atoms they were linked to (1.5 times for methyl groups). Space groups were determined based on the systematic absences and the statistical indicators, such as the E -value and the CFOM values. The absence of higher symmetry was further confirmed by Platon/Addsym. Unit cell information from ambient pressure PXRD experiments was used to help select an appropriate data collection strategy. Atomic displacement parameter plots of alkylammonium cations are provided in Supplementary Fig. 19 and Extended Data Fig. 5, and hydrogen bonding geometry of (DA)₂MnCl₄ and (NA)₂CuBr₄ are shown in Supplementary Figs. 20 and 21, respectively. Selected geometric parameters are tabulated in Supplementary Tables 11–15, and crystal data as well as details of data collection and refinement are summarized in Supplementary Tables 16 and 17. We acknowledge that there are limitations with using X-ray single crystal diffraction to determine the geometry of small organic cations in a heavy element inorganic framework, especially at high temperatures and when substantial disorder is expected to be present.

36. Arend, H., Huber, W., Mischgofsky, F. H. & Richter-Van Leeuwen, G. K. Layer perovskites of the $(C_nH_{2n+1}NH_3)_2MX_4$ and $NH_3(CH_2)_mNH_3MX_4$ families with $M = Cd, Cu, Fe, Mn$ or Pd and $X = Cl$ or Br : Importance, solubilities and simple growth techniques. *J. Cryst. Growth* **43**, 213–223 (1978).
37. Ledru, J., Imrie, C. T., Hutchinson, J. M. & Höhne, G. W. H. High pressure differential scanning calorimetry: Aspects of calibration. *Thermochim. Acta* **446**, 66–72 (2006).
38. Mañosa, L. *et al.* Giant solid-state barocaloric effect in the Ni–Mn–In magnetic shape-memory alloy. *Nat. Mater.* **9**, 478–481 (2010).
39. Lloveras, P. *et al.* Giant barocaloric effects at low pressure in ferroelectric ammonium sulphate. *Nat. Commun.* **6**, 1–6 (2015).
40. Needham, G. F., Willett, R. D. & Franzen, H. F. Phase transitions in crystalline models of bilayers. 1. Differential scanning calorimetric and X-ray studies of $(C_{12}H_{25}NH_3)_2MCl_4$ and $(NH_3C_{14}H_{29}NH_3)_2MCl_4$ salts ($M = Mn^{2+}, Cd^{2+}, Cu^{2+}$). *J. Phys. Chem.* **88**, 674–680 (1984).
41. Ricard, L., Rey-Lafon, M. & Biran, C. Vibrational study of the dynamics of *n*-decylammonium chains in the perovskite-type layer compound decylammonium tetrachlorocadmate $(C_{10}H_{21}NH_3)_2CdCl_4$. *J. Phys. Chem.* **88**, 5614–5620 (1984).
42. Almirante, C., Minioni, G. & Zerbi, G. Mechanism of solid to liquidlike phase transition of alkyl chains in bilayer systems. An infrared spectroscopic study of tetradecylammonium tetrachloromanganate $[CH_3(CH_2)_{13}NH_3]_2MnCl_4$ and tetradecylammonium tetrachlorozincate $[CH_3(CH_2)_{13}NH_3]_2ZnCl_4$. *J. Phys. Chem.* **90**, 852–859 (1986).
43. Salgado-Beceiro, J. *et al.* Near-room-temperature reversible giant barocaloric effects in $[(CH_3)_4N]Mn[N_3]_3$ hybrid perovskite. *Mater. Adv.* **1**, 3167–3170 (2020).
44. Bermúdez-García, J. M. *et al.* Giant barocaloric effect in the ferroic organic-inorganic hybrid $[TPrA][Mn(dca)_3]$ perovskite under easily accessible pressures. *Nat. Commun.* **8**, 15715 (2017).
45. Bermúdez-García, J. M. *et al.* Giant barocaloric tunability in $[(CH_3CH_2CH_2)_4N]Cd[N(CN)_2]_3$ hybrid perovskite. *J. Mater. Chem. C* **6**, 9867–9874 (2018).
46. Li, J. *et al.* Reversible barocaloric effects over a large temperature span in fullerite C_{60} . *J. Mater. Chem. A* **8**, 20354–20362 (2020).
47. Aznar, A. *et al.* Giant barocaloric effects over a wide temperature range in superionic conductor AgI. *Nat. Commun.* **8**, 1–6 (2017).
48. Lin, J. *et al.* Giant room-temperature barocaloric effect at the electronic phase transition in $Ni_{1-x}Fe_xS$. *Mater. Horiz.* **7**, 2690–2695 (2020).
49. Stern-Taulats, E. *et al.* Barocaloric and magnetocaloric effects in $Fe_{49}Rh_{51}$. *Phys. Rev. B* **89**, 214105 (2014).
50. Aznar, A. *et al.* Giant barocaloric effect in all-*d*-metal Heusler shape memory alloys. *Phys. Rev. Mater.* **3**, 044406 (2019).
51. Romanini, M. *et al.* Giant and reversible barocaloric effect in trinuclear spin-crossover complex $Fe_3(bntrz)_6(tcnsset)_6$. *Adv. Mater.* **33**, 2008076 (2021).
52. Vallone, S. P. *et al.* Giant barocaloric effect at the spin crossover transition of a molecular crystal. *Adv. Mater.* **31**, 1807334 (2019).

Supplementary Files

This is a list of supplementary files associated with this preprint. Click to download.

- [CombinedCifforDA2MnCl4.cif](#)
- [CombinedCifforNA2CuBr4.cif](#)
- [checkcifforDA2MnCl4.pdf](#)
- [checkcifforNA2CuBr4.pdf](#)
- [Supplementaryinformation.pdf](#)
- [Extendeddata.pdf](#)